Journal of Volcanology and Geothermal Research 441 (2023) 107870

Contents lists available at ScienceDirect

Journal of Volcanology and Geothermal Research

journal homepage: www.journals.elsevier.com/journal-of-volcanology-and-geothermal-research

Invited review article

Seismic anisotropy tomography beneath La Palma in the Canary Islands, Spain

I. Serrano [a,b,*], M.A. Dengra [a,b], F.J. Almendros [a,b], F. Torcal [c], D. Zhao [d]

[a] Instituto Andaluz de Geofísica, Universidad de Granada, Calle del Prof. Clavera, 12, 18071 Granada, Spain
[b] Departamento de Física Teórica y del Cosmos, Facultad de Ciencias, Campus de Fuentenueva, 18071 Granada, Spain
[c] Departamento de Sistemas Físicos, Químicos y Naturales, Universidad Pablo de Olavide, Sevilla, Ctra. de Utrera km 1, 41013 Sevilla, Spain
[d] Department of Geophysics, Graduate School of Science, Tohoku University, 980–8578 Sendai, Japan

ARTICLE INFO

Keywords:
Seismic anisotropy
Seismic tomography
La Palma (Canary islands)
Volcano
Local earthquakes

ABSTRACT

We investigated the detailed 3-D crustal structure beneath the island of La Palma (Spain) using the data from local earthquakes. We separately analyzed the pre-eruptive and the sin-post-eruptive seismic activity as well as the complete dataset. For each set we performed a separate isotropic seismic tomographic inversion to obtain isotropic 3-D P-wave and S-wave velocity (Vp, Vs) models and Vp/Vs ratio distribution down to 15 km depth. We also performed two types of anisotropic tomography using the same datasets to study 3-D Vp azimuthal and radial anisotropy structures. A high-Vp anomaly was revealed under the Taburiente caldera, which coincides with a resistive body interpreted as the oldest basal complex. In the shallower layers under the southern part of the island, low-V anomalies in the north-south direction were identified. These are associated with the N-S rift structure in Cumbre Vieja in accordance with gravity and geoelectric anomalies. Both electrical and seismic anomalies around the Cumbre Vieja volcanic ridge could indicate the presence of an active geothermal system. Just beneath the active volcano, we obtained one of the most prominent features of the seismic structure, i.e., an elongated high Vp/Vs anomaly located beneath the northwestern part of the Cumbre Vieja. These results can be interpreted as magma reservoirs containing high degrees of partial melt and/or fluids. Vp azimuthal anisotropy in the study area is mostly governed by pervasive regional and structural characteristics, for example, running parallel to the APM direction of the African plate in the western part of the island and almost parallel to the tensional stress direction in the southwestern corner. Negative Vp radial anisotropy generally appears in the crust under the Cumbre Vieja volcano down to 10 km depth. This zone is probably caused by local asthenospheric upwelling at shallow depths, possibly associated with rift-related lithospheric extension.

1. Introduction

La Palma is the north-westernmost island in the Canary Islands (Spain), rising from the 4-km deep seafloor to a height of 2430 m above sea level (Fig. 1). It has been volcanically active for at least 4 Ma. The submarine basal complex started to form about 4 Ma ago (Staudigel and Schmincke, 1984). Subaerial volcanism started about 1.8 Ma ago, with the construction of different volcanic edifices in the northern half of the island: Garafía (1.7–1.2 Ma), Taburiente-Cumbre Nueva (1.2–0.4 Ma) and Bejenado (0.56–0.49 Ma). The Taburiente edifice has been affected by huge landslides and intense erosion, exposing the submarine structure at the bottom of the Taburiente caldera (Ancochea et al., 1994). The volcanic activity migrated southward during the late stages of Taburiente, culminating in Cumbre Nueva. This volcano suffered a giant landslide on its western flank 560 ka ago (Carracedo et al., 2001). The Bejenado volcano then arose through the landslide deposits, and after a quiescent period, volcanic activity migrated southward about 123 ka ago, building Cumbre Vieja. At Cumbre Vieja, the most active basaltic volcanic field in the Canaries (Troll and Carracedo, 2016), vents are mainly located in a 20 km north-south rift reaching up to 1950 m asl.

All recent eruptions have occurred in the Cumbre Vieja volcanic field, including the prehistorical eruptions back to 6 ka (Troll and Carracedo, 2016) and the historical eruptions (Romero Ruiz, 1989). Most of them produced lava flows towards the west, although the eruption in 1644 flowed eastwards. The last eruptions occurred at San Juan in 1949 and Teneguía in 1971 (Fig. 1). San Juan involved three eruptive centers

* Corresponding author at: Instituto Andaluz de Geofísica, Universidad de Granada, Calle del Prof. Clavera, 12, 18071 Granada, Spain.
E-mail addresses: inmasb@ugr.es (I. Serrano), ftormed@upo.es (F. Torcal), zhao@tohoku.ac.jp (D. Zhao).

https://doi.org/10.1016/j.jvolgeores.2023.107870
Received 19 December 2022; Received in revised form 2 July 2023; Accepted 10 July 2023
Available online 22 July 2023

and seismicity was felt years before the eruption (Romero Ruiz, 1989). Petrological studies revealed the occurrence of three magma-mixing events matching the timescales of the unrest activity (Spica et al., 2017). The Teneguía eruption originated as a fissure near a phonolite dome and was also accompanied by intense seismicity (Barker et al., 2015).

After the 1971 Teneguia eruption, Cumbre Vieja remained fairly quiet for about 46 years. The only evidences of volcanic activity were CO2 emissions within the Taburiente caldera and some geothermal manifestations in the southern part of the island. In October 2017 the first evidence of a magmatic reactivation appeared with the renewal of seismic activity beneath Cumbre Vieja (Torres-Gonzalez et al., 2020), although previous signs of unrest have been also identified (Padrón et al., 2015, Fernandez et al., 2021). Seismic swarms continued until August 2021, with epicenters located at ~20 km depth. On September 11, 2021 a new seismic swarm started at a depth of 10 km on the eastern flank of Cumbre Vieja. In the next few days, the seismicity migrated westward and ground deformation began to be clearly detected. On September 18, 2021 the depth of seismicity fell sharply, and reached a peak magnitude of Ml 3.1 in the morning of September 19. The eruption started around 14:10 UTC on the same day from a single eruptive vent which evolved into a fissure in a few hours. The eruption continued with important explosive activity until September 27, when it came to a temporary halt. Activity resumed in the evening of the same day with a dominantly effusive style. At the beginning of October, the lava reached the sea, causing the formation of the first lava delta. Seismic activity renewed with two clusters located at depths of about 10 and 20 km. This seismicity lasted throughout the whole eruption reaching a maximum magnitude of Ml 4.1. Hundreds of earthquakes were felt, with intensities of up to IV-V EMS (Modified Mercalli Scale). From October to December, the lava field widened considerably, causing extensive damage. See e.g. Carracedo et al., 2022 and Romero et al., 2022 for a detailed description and timeline of the eruption.

In this paper, we investigate the anisotropic seismic structure under Cumbre Vieja volcano, making use of an anisotropic tomography inversion of local earthquake travel times. Seismic tomography is a widely used tool in volcanoes (Lees, 2007; Koulakov and Shapiro, 2015), since it provides insight into the three-dimensional distribution of the velocity structure and can help us understand the spatial characteristics of the magma accumulation zones and magma pathways. In La Palma, seismic tomography has been performed using ambient noise (Cabrera-Perez et al., 2021) and local earthquakes (D'Auria et al., 2022). However, anisotropy is also an important characteristic of volcanic environments (Johnson, 2015; Chouet and Matoza, 2013). Seismic anisotropy is related to the state of stress, and therefore it can reveal subtle changes in the dynamics of volcanic systems (Gerst and Savage, 2004, Konstantinou et al., 2013, Llsley-Kemp et al., 2018, Saade et al., 2019). In the last years, there has been an effort to include anisotropy into the tomography inversion schemes (e.g. Koulakov et al., 2009, Mordret et al., 2015, Jiang et al., 2018, Lu et al., 2022, De Plaen et al., 2022, Hudson et al., 2023, Perton et al., 2022). In this way, tomography can be performed avoiding the over-simplifying hypothesis of isotropy, that might introduce significant velocity artifacts that could be misinterpreted as compositional and/or thermal heterogeneities (Lo Bue

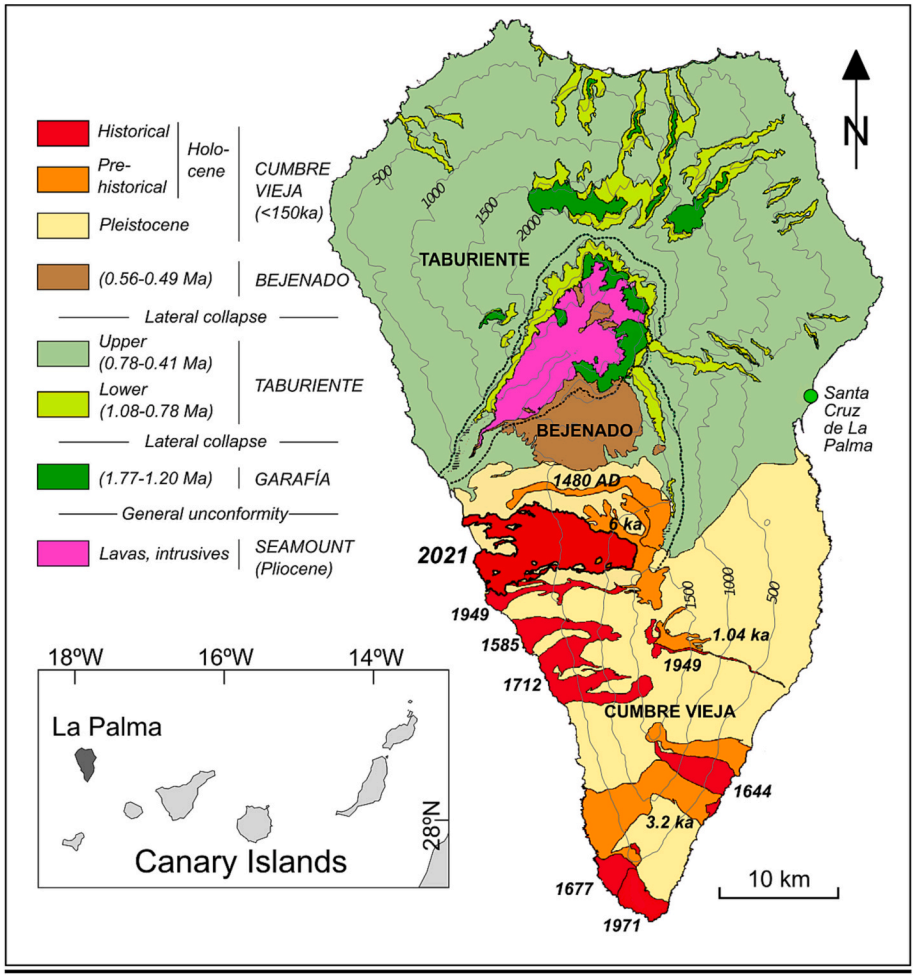

Fig. 1. Map of La Palma showing the different stratigraphic units and the lava flows from Cumbre Vieja volcano (after Troll and Carracedo, 2016); the 2021 lava flow contour (thick line) was obtained from Civico et al. (2022).

et al., 2023). Our objective is to estimate the three-dimensional distribution of seismic velocity and anisotropy under Cumbre Vieja volcano, compare this distribution with the results obtained using different geophysical methods, and address what consequences it may have in our understanding of the structure and dynamics of the Cumbre Vieja magma plumbing system.

2. Data and methods

Our study period covers twelve years of seismic activity recorded at La Palma island between January 2010 and February 2022, containing different stages of activity at the Cumbre Vieja volcano. The data used was from local events recorded at 20 temporary and permanent seismic stations in La Palma (Canary Islands, Spain) collected from the *Instituto Geográfico Nacional* (*IGN*, Spain). All the data are publicly accessible from the Data Management Center of the Incorporated Research Institutions for Seismology. This seismic network provided dense, uniform coverage over the course of the study period, except for isolated areas in the northern and southern islands, where there are fewer stations. The interpretation of our results depends on the resolution of the isotropic and anisotropic images, which is directly related to the number of earthquakes and seismic stations as well as the seismic ray coverage in the modeled volume. This means that some regions have been interpreted in greater detail than others.

The earthquakes were selected on the basis of the number of arrival times and the accuracy of the hypocenter locations as well as a local velocity model beneath the island. Most of the earthquakes were recorded at five or more seismic stations in different parts of the island. The investigated area covers a total of 1045 km^2. The depth range is from 1 to 15 km. For the *IGN* stations, the accuracy of time picking may be estimated in the most favorable cases as 0.01 s. In the case of less impulsive arrivals and/or poor signal-to-noise ratio, the accuracy is degraded. All the events used in this study had magnitudes of <5.0 mbLg. Fig. 2 shows the relationship between the P- and S-wave travel times of the earthquakes used in this study. The correlation coefficient (R^2) was 0.99.

Our entire data set contains 325,091 P-wave arrivals and 362,638 S-wave arrivals from 38,777 local earthquakes with an average uncertainty of 1.24 km, 1.06 km and 1.27 km in latitude, longitude and focal depth, respectively (Table S1).

For the initial entire data set, the average uncertainty of their origin times is reduced after three iterations from 0.94 s. to 0.20 s. After the earthquake relocation, the root-mean-square (RMS) travel-time residual is reduced from 0.26 s to 0.24 s for P-wave arrivals and from 0.31 s to 0.30 for S-wave arrivals. Fig. 3 shows the distribution of all the events after the relocation process (Fig. S1 shows the distribution of all the events before the relocation process).

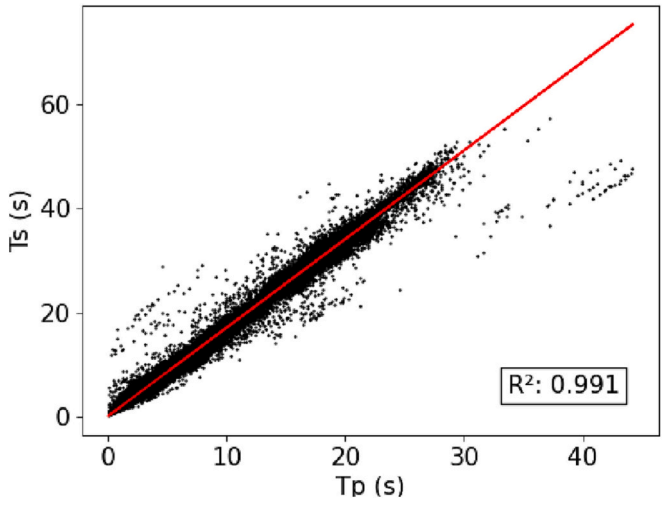

Fig. 2. Relationship between the P- and S-wave travel times of the earthquakes used in this study. The correlation coefficient (R^2) is 0.99.

We used a 1-D realistic velocity model of the crust and upper mantle for the island of La Palma, which was derived from the model developed by Dañobeitia (1980). This 1-D model is the same as the one used to obtain the catalog of hypocenters. The velocity model contains three layers: from 0.0 to 4.0 km (Vp = 4.2 km/s), from 4.0 to 12.0 (Vp = 6.3 km/s) and from 12.0 to 18.0 (Vp = 7.0 km/s). Vp/Vs is set at 1.78 in the initial model.

A total of nine seismic inversions were carried out (Table S1): isotropic inversions (Model 1) for the pre-eruptive database (first inversion), for the *syn*-post-eruptive database (second inversion) and for the complete database (third inversion), azimuthal anisotropic inversions (Model 2) for the pre-eruptive database (fourth inversion) for the syn-post-eruptive database (fifth inversion) and for the complete database (sixth inversion), and radial anisotropic inversions (Model 3) for the pre-eruptive database (seventh inversion) for the syn-post-eruptive database (eighth inversion) and for the complete database (ninth inversion). In each case, before conducting the inversion, we relocated the events of each database and estimated the uncertainties of the hypocentral parameters using an iterative least-squares method [Geiger, 1910, 1912; Zhao et al., 1992].

2.1. Isotropic seismic tomography

In this study we applied the tomographic method proposed by Zhao et al. [1992]. Although the conceptual approach of this method parallels that of (Aki and Lee, 1976; Albert et al., 2016), it also incorporates some additional features [Zhao et al., 1992; Zhao, 2015]. The medium we studied is divided into layers by three velocity discontinuities. Three-dimensional grid nodes are arranged in every layer. Velocities at grid nodes are taken to be unknown parameters. The velocity at any point in the model is calculated by linearly interpolating the velocities at the eight grid nodes surrounding that point. The nonlinear tomographic problem is solved by iteratively conducting linear inversions until a convergent solution is found. We used the efficient 3-D ray tracing technique proposed by Zhao et al. (1992) to trace rays between hypocenters and seismic stations and calculate theoretical travel times and travel time residuals.

The final model was parameterized by a 3-D grid with grid intervals of 0.02° (≈ 2.2 km) by 0.02° (≈ 2.2 km) by 2 km (latitude x longitude x depth). The grid interval depends on the number of rays passing through the model, and is therefore obtained from the results of the resolution tests. The minimum hit count, i.e. the number of rays passing through each grid node, is 10. The number of nodes is 19 in the latitude direction, 13 in the longitude direction and 9 in depth. The total number of grid nodes is 2223.

The Vp, Vs and Vp/Vs ratio may be sensitive to factors that can change over time before and after the volcanic eruption. This means that time-dependent seismic tomography may be used to reveal variations in the elastic properties within rock volumes. For this reason, we separately analyzed the pre-eruptive (4 January 2010 to 18 September 2021) and the *syn*-post-eruptive (19 September 2021 to 25 February 2022) seismic activity. For each dataset, we performed a seismic tomographic inversion (first and second inversions) and then calculated the distribution of the Vp/Vs ratio. For the pre-eruptive data set, a total of 30,149 earthquakes with 197,071 P-arrivals and 224,615 S-arrivals were inverted, with a final RMS travel-time residual of 0.22 s for P and 0.26 for S arrivals. Subsequently for syn-post-eruptive data, a total of 8628 earthquakes with 128,020 P-arrivals and 138,023 S-arrivals were inverted, with a final RMS travel-time residual of 0.27 s for P-wave data and 0.33 s for S-wave data.

For the first dataset, we solved the inverse problem with 3514 velocity parameters (1641 for Vp and 1873 for Vs) at the grid nodes with hit counts >10. For the second dataset, there were 2795 velocity

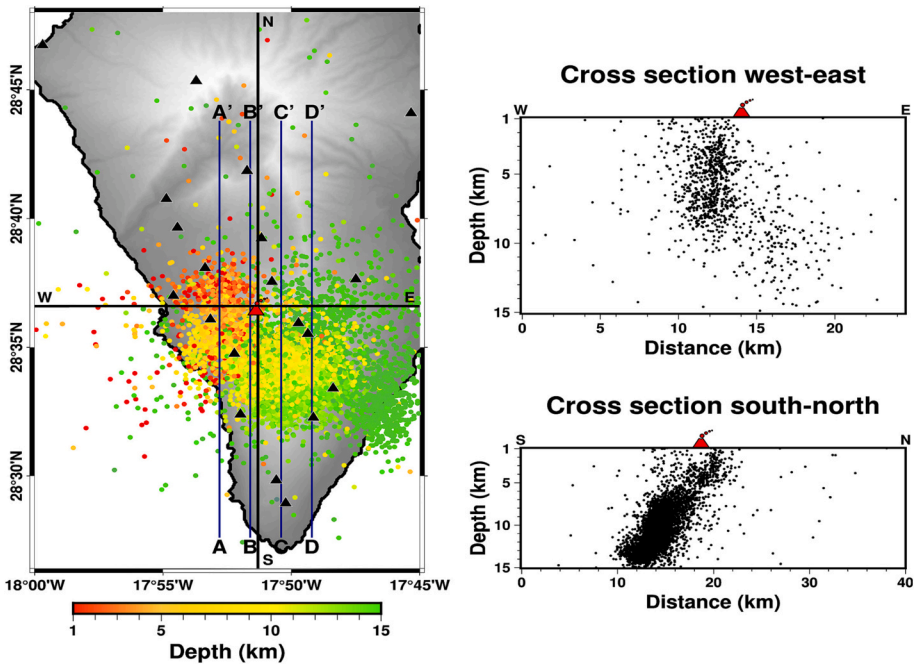

Fig. 3. Distribution of the 38,777 earthquakes (colored dots) and 20 stations (black triangles) used in this study. The colour shows the focal depth whose scale is shown at the bottom. The black lines running N-S and *E*-W mark the locations of the vertical cross-*sec*tions on the right, which show the distribution of seismicity in depth. Lines A'-A, B′-B, C′-C and D′-D correspond to the cross sections of Figs. 5, 7, S7, S8 and S10.

parameters (1338 for Vp and 1457 for Vs).

It is very important to note that the analysis of the seismic catalog confirmed the tendency of the seismicity to cluster in space during and after the eruption, which explains why more grid nodes were sampled before the eruption occurred.

Later, we performed an isotropic tomographic inversion of the whole dataset from 4 January 2010 to 25 February 2022 to determine 3-D Vp and Vs images (third inversion). For the isotropic seismic tomography with the entire database a total of 38,777 earthquakes were inverted. We solved the inverse problem for 3718 velocity parameters (1754 for Vp and 1964 for Vs) at the grid nodes with hit counts >10.

Some of the grid nodes are well sampled by the rays, while others are poorly sampled. Hence, damping regularization is required to stabilize the solution, whose stability is determined by comparing the data variance with the model variance. The damping parameter was selected on the basis of an empirical approach (Eberhart-Phillips, 1986). A number of inversions were conducted with different damping values. The reduction in the travel time residual was then compared to the variance in the solutions and a tradeoff curve was drawn between the two. The value selected as the damping parameter for the entire dataset is the one that gives the optimal residual reduction and solution variance (Fig. 4). According to Lin et al. (2007) decreasing the damping parameter could increase the resolution throughout the grid space, but the velocity results may be less reliable.

We then determined the 3-D distribution of Vp/Vs for each of the three inversions. It is important to note that we only show results at nodes where we have both Vp and Vs values.

2.2. *P-wave tomography for azimuthal and radial anisotropy*

After obtaining the results of the isotropic inversion, we carried out the anisotropic tomographic inversions separately. In other words, we began by conducting an inversion for the 3-D isotropic Vp and azimuthal anisotropy structures, and then performed an inversion for the 3-D isotropic Vp and radial anisotropy structures of La Palma. First of all, it is important to emphasize that the azimuthal and radial anisotropic inversions represent two fundamentally different assumptions regarding

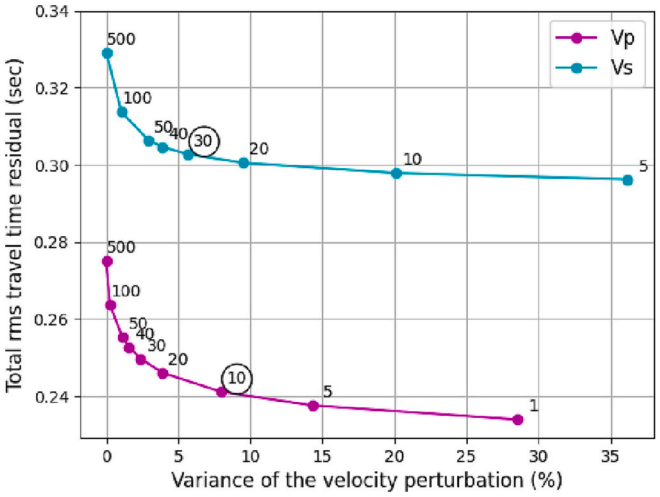

Fig. 4. (A) Trade-off curve between the variance of the velocity perturbation (in percentage) and the total RMS travel time residual (sec) for different damping parameters, from 1 to 500. The selected value for the final results is marked inside the circle, 10 for P waves and 30 for S waves.

the nature of anisotropy and, consequently, about how it is interpreted (1) the azimuthal model assumes a horizontal symmetry axis (e.g., vertical fracture planes) while (2) the radial model assumes a vertical symmetry axis (e.g., horizontal layering). The results from these two end-member assumptions, together with the isotropic inversions, illustrate the extent to which isotropic Vp heterogeneity may be counterbalanced by anisotropic structure. Moreover, according to Zhao and Hua (2021), direct comparison of the azimuthal anisotropy and radial anisotropy models should be done carefully for the following two reasons. (1) The two models are independently derived and it is unclear what the trade-offs are between the azimuthal and radial parameters. Their trade-offs may be due to a dip in the symmetry axis (i.e., apparent anisotropy). (2) The resulting isotropic Vp images show some

differences, suggesting that the interplay between the isotropic and anisotropic structures is also unknown, partly due to the imperfect ray coverage (e.g., Hsin-Hua and Huang, 2015). In the isotropic inversion, the effects of azimuthal and radial anisotropic models are mapped into the isotropic Vp image. The inhomogeneity of the angular coverage of the ray paths may produce an apparent anisotropy (Ishise et al., 2012). In the azimuthal and radial inversions, the contributions of seismic anisotropy to the travel-time residuals are separated, at least partially, from the isotropic Vp image. As a result, the three isotropic Vp models display some differences in the amplitude and spatial extent of Vp anomalies. These differences in the isotropic Vp image may reflect the greater effect of seismic anisotropy on the structure of the study area.

According to Anderson (1989), the most obvious manifestations of seismic anisotropy in the crust and upper mantle of the Earth are: shear-wave birefringence -the two polarizations of S-waves arrive at different times-, azimuthal anisotropy -the arrival times, or apparent velocities of seismic waves at a given distance from an event, depend on the azimuth-, and finally, an apparent discrepancy between Love and Rayleigh waves. He pointed out that seismic velocity variations due to anisotropy are potentially much greater than those due to other effects such as composition and temperature. Hence, it is important to understand anisotropy well before attempting to infer chemical, mineralogical and temperature variations from seismic data. A change in the preferred orientation with depth or from one tectonic region to another can be easily misinterpreted. These theoretical considerations are perfectly applicable to volcanic environments, for example, any overpressured magma storage reservoir, be it a system of dikes, sills, conduits, spherical chambers, or a combination of these, will exert a stress on the surrounding country rock that may or may not manifest itself as observable strain (Johnson, 2015). One indicator of stress change in the crust around a volcano is the occurrence of volcano-tectonic earthquakes. Changes in the stress field may trigger more volcano-tectonic events, the detection of which is one of the most successful seismic volcano monitoring tools.

Hearn (1996) developed a method to simultaneously solve for 2-D velocity and azimuthal anisotropy from Pn travel time residuals and applied it to the western United States. Eberhart-Phillips and Henderson (2004) developed a method that extends Hearn's (1996) technique, by implementing azimuthal anisotropy in a simultaneous inversion for 3-D seismic velocity and hypocenters. They added two anisotropic parameters at each velocity node, applying the following equation (Backus, 1965; Raitt et al., 1969) for characterizing weak azimuthal anisotropy for P waves:

$$S(\varnothing) = S_0 + A\cos(2\varnothing) + B\sin(2\varnothing) \quad (1)$$

where S is the anisotropic slowness, S_0 is the azimuthal average slowness (i.e. isotropic component), ϕ is the ray path azimuth and A and B are anisotropy parameters. The fast velocity direction (FVD, or anisotropic azimuth) is expressed as follows:

$$\psi = \frac{1}{2}tan^{-1}\left(\frac{B}{A}\right) + \begin{cases} \pi/2, A > 0 \\ 0, A < 0 \end{cases}$$

The magnitude of the anisotropy can be described in terms of the A and B values shown in eq. (1) or in terms of the fast direction and the total anisotropy, M, or the percentage of anisotropy, α.

$$M = \sqrt{A^2 + B^2}$$

$$\alpha = \frac{V_f - V_s}{V_0} = \frac{2M}{S_0 - M^2/S_0}$$

where V_f and V_s are the velocities in the fast and slow directions.

Fracture-induced anisotropy has a slow symmetry axis, making the assumption of a fast symmetry axis inappropriate in this case.

Following this approach, we applied the tomographic method for Vp azimuthal anisotropy (Wang and Zhao, 2008, 2013) that was developed from the isotropic tomography method proposed by Zhao et al. (1992). This anisotropy method is similar to that of Eberhart-Phillips and Henderson (2004), but it can deal with complex geometries of velocity discontinuities such as the Conrad and Moho discontinuities in the study volume. A horizontal hexagonal symmetry in the modeling space is assumed and two anisotropic parameters (A and B) at each grid node are considered in addition to the isotropic Vp parameter.

In line with Ishise et al. (2012), in Vp radial anisotropy tomography, we assumed that the symmetry axis was vertical and estimated both the anisotropic strength and the 3-D isotropic velocity structure. The unknown parameters were isotropic Vp perturbation and a dimensionless parameter to describe the anisotropic strength. It should be noted that the hexagonal symmetry considered here corresponds to that with the elliptic condition (Kawakatsu, 2016; Thomsen, 1986). In this study, we applied the code developed by Wang and Zhao (2013) to determine the 3-D Vp radial anisotropy of the study region.

To this end, we set up a 3-D grid with a lateral grid interval of 0.03° and a vertical grid interval of 2 km to express the 3-D azimuthal and radial anisotropy (from fourth to ninth inversions), because seismic anisotropic tomography needs better ray coverage and crisscrossing than isotropic tomography. We used the same initial velocity model, smoothing and damping and the same amount of seismic rays as for the isotropic tomography. The dependency of the variance reduction on the damping factor is similar for the different inversions. For P waves we solved the azimuthal inverse problem for 610, 262 and 462 velocity parameters (fourth, fifth and sixth inversions respectively, Table S1) and the radial inverse problem for 519, 197 and 353 velocity parameters (seventh, eighth and ninth inversions respectively), at the grid nodes with hit counts >10.

In the same way as in isotropic inversions, it is important to take into account the tendency of seismicity to cluster in space during and after the eruption, which explains why more grid nodes were sampled before the eruption occurred.

3. Resolution tests

The first step was to analyze the seismic rays crossing the whole area with the complete dataset to obtain an indication of the resolution in the study area. Zones with many crossing rays are better sampled than zones that contain just a few. Fig. S2 shows, for the isotropic P inversion, the distribution of the number of P-wave rays passing near each grid node, the "hit counts" for the eight layers. We can see that the coverage is good down to 15 km depth in the central and southern parts of the island, where the highest hit count was observed. The absence of seismic stations in the northern part of the island results in very poor control of its velocity structure.

To examine the resolution scale of the data set, we carried out a checkerboard resolution test (CRT), the test normally used to assess resolution in tomographic inversions. One direct way to evaluate the resolution of a tomographic result is to calculate the set of travel time delays that result from tracing the corresponding rays through a synthetic structure, and then compare the inversion result with the initial synthetic structure (Zhao et al., 1992). In the synthetic tests, the numbers of stations, events, and ray paths are the same as those in the real data set. In this study we conducted a kind of resolution test to assess the adequacy of the ray coverage and evaluate the resolution. The checkerboard resolution test can be viewed as a special form of synthetic test. The only difference between them is in the input model (Fig. S3). To make a checkerboard, positive and negative 6% velocity perturbations are assigned to the 3-D grid nodes arranged in the modeling space. In this study, many such tests were performed by adopting different grid intervals. We found that the optimal grid interval for the tomographic inversion of our data set was 0.02° x 0.02° in the horizontal directions. In this optimal model we set the grid nodes at depths of 1, 3, 5, 7, 9, 11, 13, 15 and 18 km. The grid interval in the crust was determined by the seismic distribution in the area and the fact that the majority of

earthquakes are shallow. The images in Figs. S4 and S5 show the results of the resolution tests for P and S waves for eight layers up to 15 km depth from the complete data set. The shallower parts of the study area have a higher resolution because the local rays crisscross well in the uppermost crust.

We also performed CRTs to test the results obtained by Vp azimuthal and radial anisotropic tomography. In the input model for the CRTs used for azimuthal anisotropy tomography, the FVDs at two adjacent grid nodes are perpendicular to each other (22.5° and 112.5°) with an anisotropic amplitude of 5.0% (Fig. S6). The red and blue bars indicate the input and output FVDs of Vp azimuthal anisotropy, whose length indicates the anisotropic amplitude. Random errors in a normal distribution with a standard deviation of 0.1 s were added to the theoretical arrival times calculated for the CRT input model.

The results of the CRTs for Vp radial anisotropy tomography are presented in twelve vertical cross-sections for the three subsets of earthquakes in Fig. S7. This figure corresponds to three independent CRTs for three data subsets: first column, for the time period before the start of eruption (seventh inversion), second column, for the data obtained during and after the eruption (eighth inversion) and third column, for the complete database (ninth inversion). In the input model for the CRT for Vp radial anisotropy (RAN), 5.0% positive and negative RANs were alternatively assigned to the adjacent grid nodes. The thin red bars show the RANs in the input model, while the blue bars indicate the RANs recovered after the tomographic inversion. Random errors in a normal distribution with a standard deviation of 0.1 s were added to the theoretical arrival times calculated for the CRT input model.

4. Results

Model 1, isotropic tomography, has Vp, Vs and therefore Vp/Vs data. We have much more data and therefore more results than in Model 2 and Model 3 and can make a much more extensive interpretation than with the other two models. Model 1 has the best spatial resolution of the three models: 0.02° x 0.02° x 2 km (latitude x longitude x depth) and in some ways it is the most reliable. Model 2, azimuthal anisotropy, only has Vp data, so offering less data than in Model 1 and making our interpretation more limited. In addition, more data is needed to calculate the azimuthal anisotropy, and the grid spacing must be larger. As a result, it has a lower resolution than the previous model: 0.03° x 0.03° x 2 km (latitude x longitude x depth). For Model 3, radial anisotropy, something similar to Model 2 occurs, we have less data and the resolution is lower than for

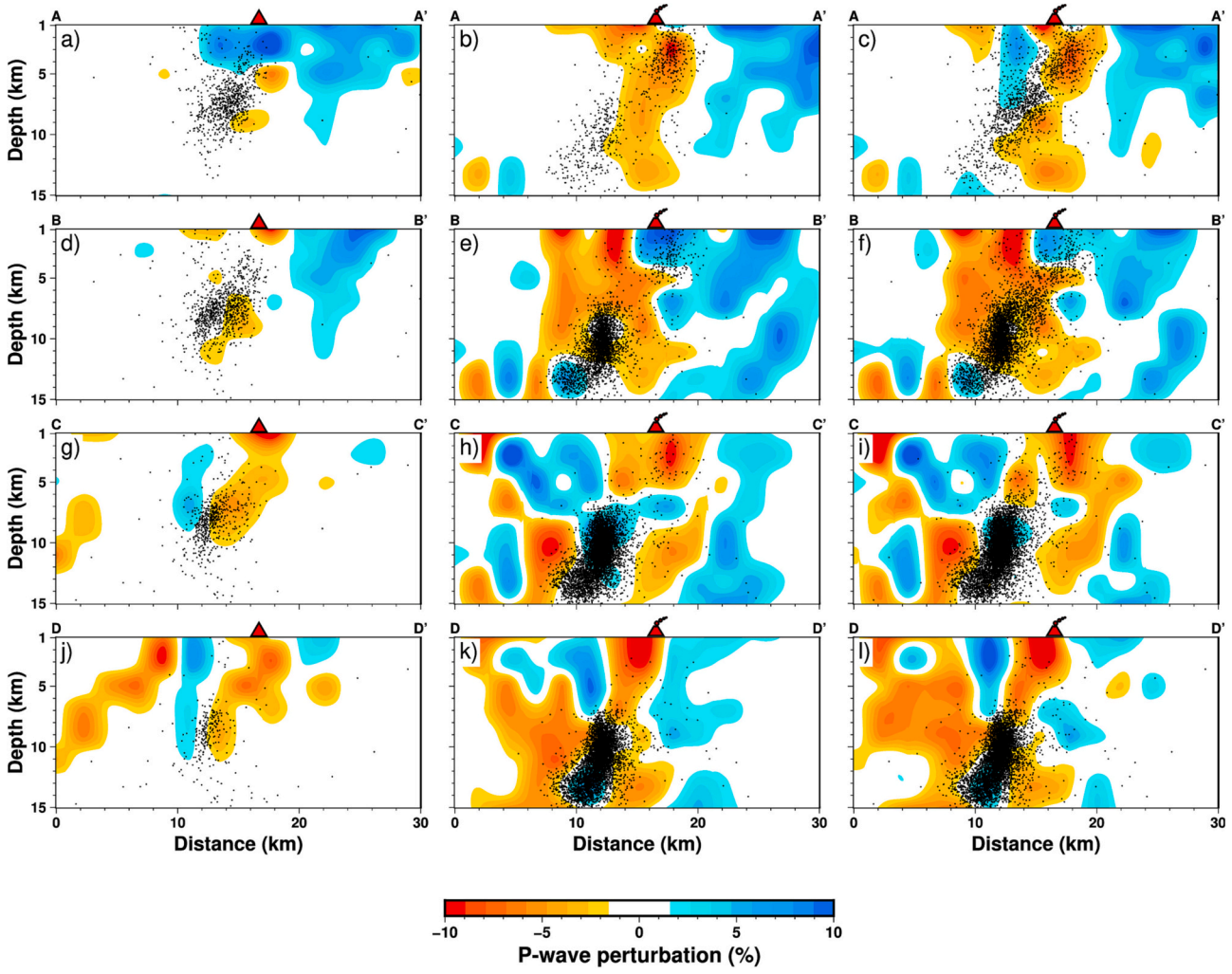

Fig. 5. S-N vertical cross-sections of Vp tomography at depths of 1–15 km (shown by letters A-A', B-B′, C-C′ and D-D′ in Fig. 3). Red and blue colors indicate slow and fast velocities, respectively. The red triangle indicates the active volcano. Earthquakes within a 5-km width from the cross-section are shown with black dots. The velocity perturbation scale is shown at the bottom. This figure corresponds to three independent inversions for three data subsets: first column (a, d, g and j), for the time period before the start of the eruption (first inversion), second column (b, e, h and k), for data obtained during and after the eruption (second inversion) and third column (c, f, i and l), for the complete database (third inversion). (For interpretation of the references to colour in this figure legend, the reader is referred to the web version of this article.)

Model 1.

All our tomographic models show strong inhomogeneities in the crust beneath the study region, as expected in a volcanically active region. First, we focus on the results obtained from the inversion for the isotropic Vp and Vs structure and hypocenter relocation in the study area to 15 km depth. From these results we obtained the 3-D Vp/Vs ratio distribution. Given the good resolution obtained in the central and southern parts of the island, we will mainly be discussing the features revealed in these areas. However, it should be noted that anisotropy was only considered for P-waves and that P- and S-waves have different sensitivities to anisotropic structure, which could bias the estimated Vp/Vs ratios.

Fig. 5 shows twelve vertical cross-sections of Vp perturbations (in percentage) in the S-N profiles (A-A', B-B′ etc.) in Fig. 3, including the background seismicity (black dots) within ±5 km distance of the profile line. Blue and red colors indicate fast and slow velocities, respectively. The Vp perturbation is from the mean value of the inverted velocity at each layer. The Vp perturbation scale is shown at the bottom of the figure. This figure corresponds to three independent inversions for three data subsets, as in Fig. S6: first column (before the start of the eruption), second column (during and after the eruption) and third column (complete database). Fig. S8 is the same as Fig. 5 but for Vs tomography.

It is important to note that most of the events from our database occurred during the main period of unrest. These models therefore represent the state of the volcano just before the start, during and after the eruption. It is important to bear in mind that the number of seismic stations was increased in the weeks immediately prior to the beginning of the eruption, and that this may have distorted the results slightly because more data was available than in previous months. In Fig. 6 we can see Vp perturbations at the eight depth layers from the complete database (before and after the eruption). The depth of the layer is shown in the bottom-left corner of each map. The black line shows the coast line. Again Fig. S9 is the same as Fig. 6 but for Vs tomography.

In relation to the 1-D model, velocity anomalies range from −6.89% to +7.0% for P-waves and from −7.62% to +7.54% for S-waves for 95% of the 2223 nodes in the studied volume.

In the shallowest layers, a strong high-Vp anomaly can be seen under the Taburiente caldera. This anomaly, located in the northwestern part of the study area, is robustly sampled in all time periods and can be seen in all horizontal and vertical sections. In the southern half of the island, from 1 to 3 km depth, strong low-Vp anomalies aligned in a north-south direction are obtained.

From the results of the first cluster of earthquakes, before the eruption (first inversion), the velocity anomalies range from −4.99% to +4.07% for Vp and from −3.42% to +3.63% for Vs for 95% of the nodes in the study volume. From the second cluster of earthquakes (second inversion), during and after the eruption, the velocity anomalies range from −6.35% to +7.05% for P-waves and from −6.29% to +6.94% for S-waves for 95% of the nodes in the study volume. Fig. 5 shows big differences in seismic velocity around the volcano region: in the A-A' cross-sections (a and b images) a dramatic change in Vp from high to low values before and after eruption is obtained in the same area down to 5 km depth. However, under the volcano, the B-B′ cross-sections (d and e images) show low velocities from the first cluster and high velocities

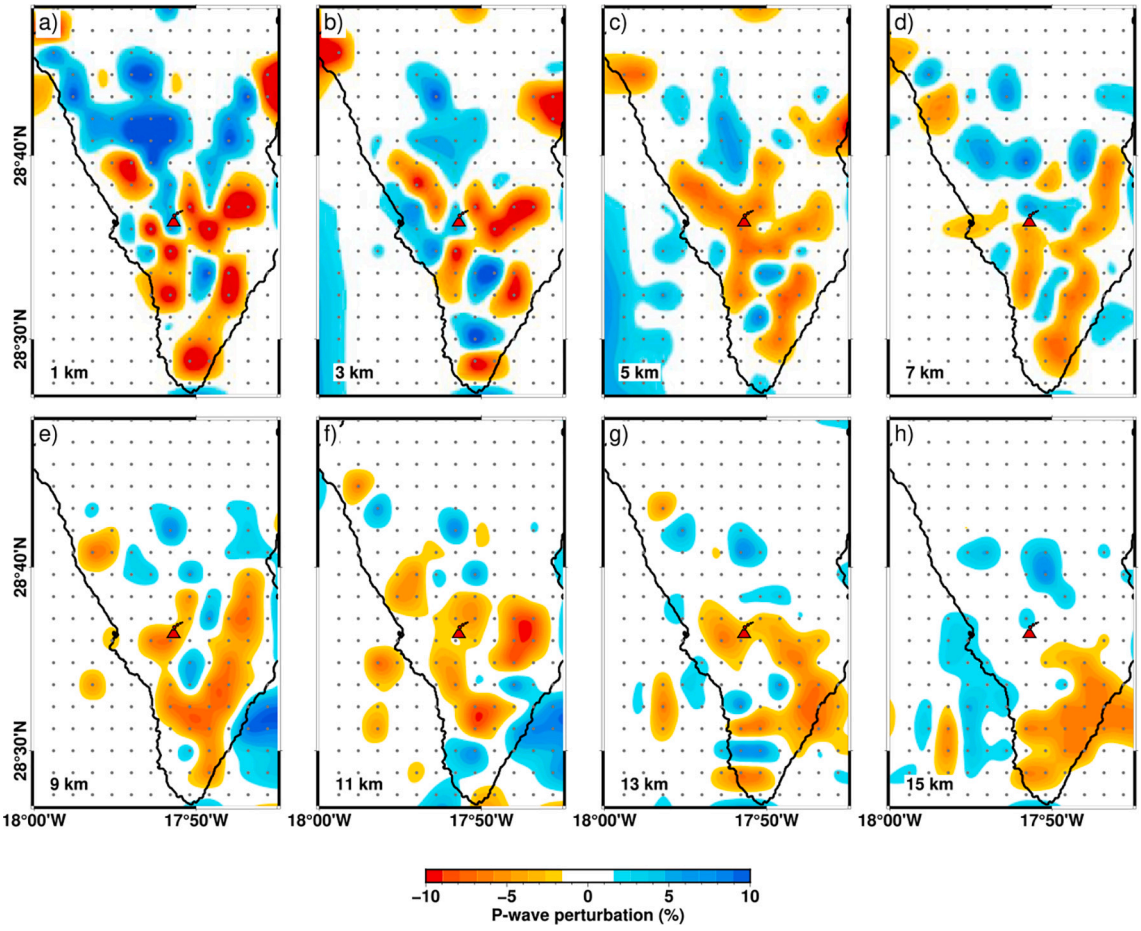

Fig. 6. Fractional Vp perturbations (in percentage) at eight depth layers obtained from the complete database. The Vp perturbation is from the mean value of the inverted velocity at each depth. Red and blue colors indicate slow and fast velocities, respectively. The Vp perturbation scale is shown at the bottom. The black line marks the coast line of La Palma. The black dots are the grid nodes in every layer. (For interpretation of the references to colour in this figure legend, the reader is referred to the web version of this article.)

from the second. In any case it is clear from the second and third clusters (third inversion) that the Cumbre Vieja volcano is situated in a high-V anomaly surrounded by low-V anomalies to 5 km depth. In this same area in the southern part of the island, the results for Vs are similar near the volcano.

The resulting distributions of the Vp/Vs ratio are presented in twelve vertical cross-sections for the three subsets of earthquakes in Fig. 7, as also in Fig. 5. The location of the profiles is shown in Fig. 3, including the background seismicity (black dots) within 5 km distance of the profile lines. We only calculated the Vp/Vs ratio for the nodes for which we had both Vp and Vs results. As a result, we only show the nodes with hit counts of >10 (for both P- and S-waves) because these results are considered sufficiently robust. On the basis of these assumptions, we obtained results in 1517 nodes of the modeled volume. In 95% of these nodes the ratio values were between 1.63 and 1.92 for the complete database (third inversion). For the pre-eruption cluster, we obtained results in 1430 nodes. In 95% of these nodes the Vp/Vs ratios were between 1.68% and 1.86%. For the *syn*-post-eruption cluster, we obtained 1150 nodes, in 95% of which the Vp/Vs ratios were between 1.63 and 1.93.

Vp/Vs images are more difficult to interpret than Vp and Vs images, but some meaningful features can be identified. From the second and third inversion results, the A-A' and B-B′ vertical sections (b, c, e and f images in Fig. 7) demonstrated a prominent anomaly in the high Vp/Vs ratio in the shallower layers, which reached a value of >2.0 concentrated beneath the northwestern part of the Cumbre Vieja volcano. This high Vp/Vs ratio is clearly visible at 1 and 3 km depth in Fig. 8, which shows the results for individual layers, and it disappears at a depth of about 5 km. This anomaly in the Vp/Vs ratio was not obtained before the beginning of eruption (first inversion).

From C-C′ and D-D′ vertical cross-sections in Figs. 5 and 7 (h, i, k and l images), a finger-shaped anomaly in the second and third clusters of data can be observed dipping to the south with a high-Vp and a low Vp/Vs ratio. This anomaly is surrounded by low Vp. Vs is not high either.

Fig. 9 shows map views of the Vp azimuthal anisotropy tomography at eight layers in the crust under the study area (Table S1, sixth inversion). The azimuth and length of each bar represent the Vp FVD and anisotropy amplitude, respectively. We performed anisotropic seismic inversion for the P waves. Our results led us to conclude that similar Vp structures were obtained in both the anisotropic and isotropic inversions, which suggests that the simultaneous inversion of the average velocity and anisotropic parameters conducted here does not affect the recovery of velocity heterogeneity. In addition, no significant differences were observed in the results from the first and second clusters of data. We therefore decided to examine the FVDs arising from the complete data set. The amplitude of the Vp azimuthal anisotropy is <4.59%

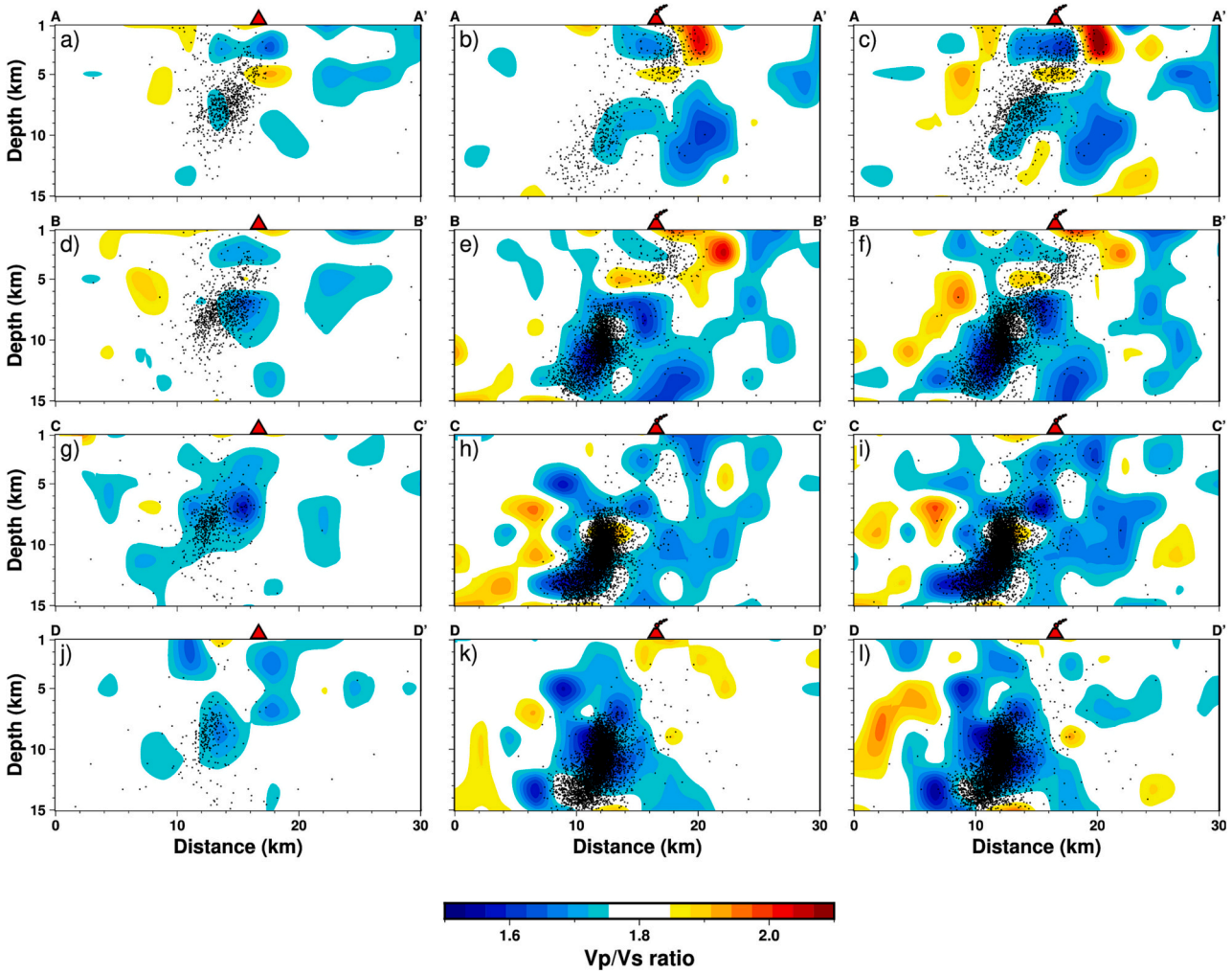

Fig. 7. Distributions of the Vp/Vs ratio in twelve vertical cross sections for the three subsets of earthquakes similar to Fig. 5. Locations of the profiles are shown in Fig. 3, including the background seismicity (black dots) within a 5-km width of each profile. The Vp/Vs ratio was only calculated for those nodes where we have both Vp and Vs results. As a result, we only show the nodes with hit counts of >10 (for both P- and S-waves) because these results are considered sufficiently robust. The scale is shown at the bottom. Blue and red colors indicate low and high Vp/Vs ratios, respectively. (For interpretation of the references to colour in this figure legend, the reader is referred to the web version of this article.)

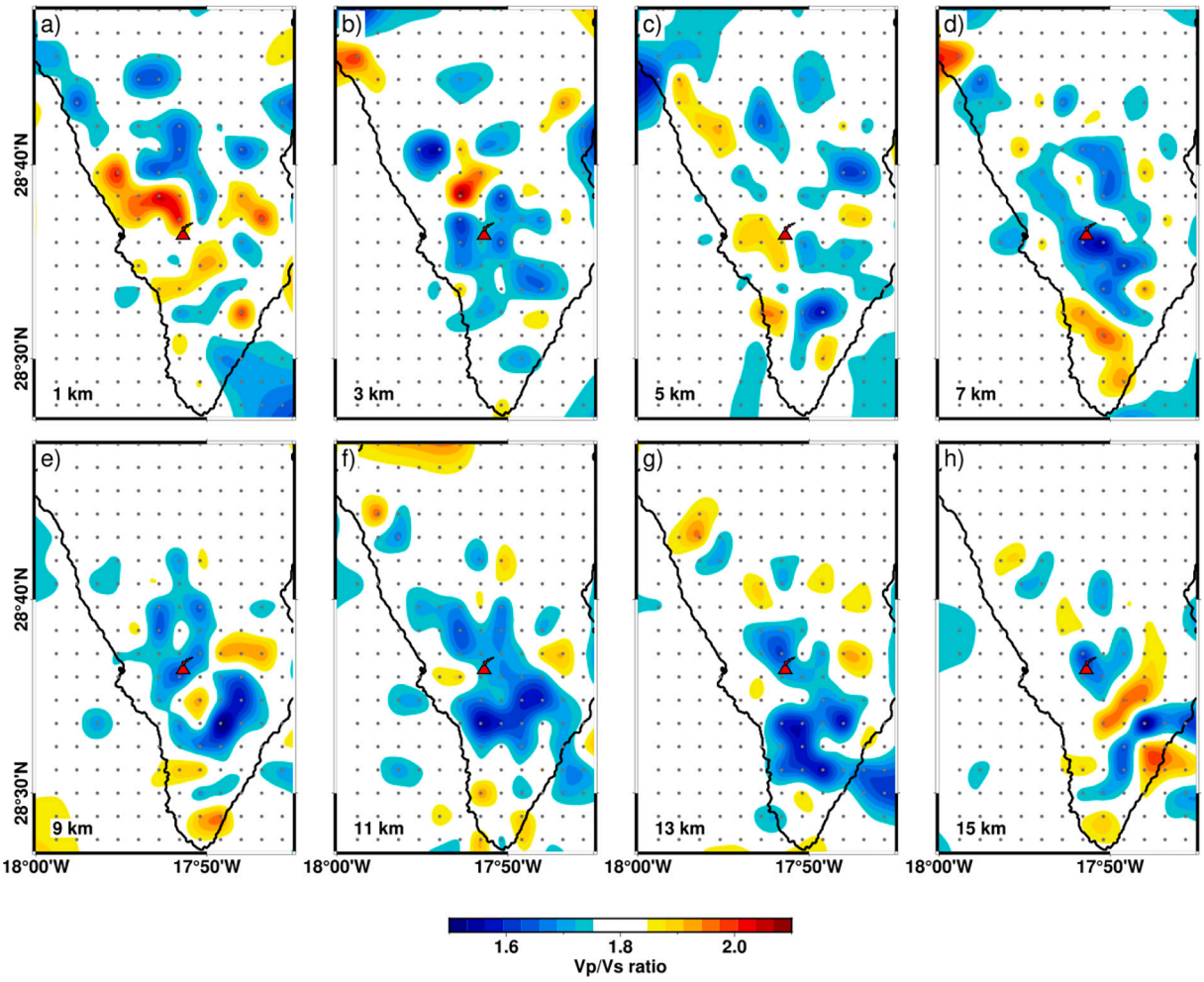

Fig. 8. Map views of the Vp/Vs ratio at eight depth layers derived from the complete data set. The scale is shown at the bottom. Blue and red colors indicate low and high Vp/Vs ratios, respectively. (For interpretation of the references to colour in this figure legend, the reader is referred to the web version of this article.)

in the study area for 95% of the total nodes. Our results in the central western part of the study area show that the FVD is mostly *E*-W from 1 to 3 km depth and nearly NE-SW from 9 to 15 km depth. However, the FVDs revealed on the eastern flank of the ridge exhibit mainly NW-SE directions from 9 to 11 km depth and turn E-W in the deepest layers. In short, it is important to note, from 9 to 15 km depth, the significant shift in direction around the axis of the Cumbre Vieja rift from NE-SW to NW-SE/E-W from west to east in the southern half of the island.

Fig. S10 shows twelve south–north vertical cross-sections of Vp radial anisotropy tomography under La Palma (Table S1, seventh, eighth and ninth inversions). For these seismic inversions, we again used the three clusters of earthquakes (before, *syn*-post eruption and complete database). The method proposed by Wang and Zhao (2013) used in this study assumes that the properties of radial anisotropy for P-wave are similar to those for S-wave. Similar to the use of the V_{sh}/V_{sv} ratio in surface-wave tomography (e.g. Nettles and Dziewoński, 2008; Fichtner, 2010; Yuan et al., 2011), in this study we use the V_{ph}/V_{pv} ratio to express P-wave radial anisotropy (RAN). From the complete set of data, negative RAN (vertical bars) generally appears in the crust under the Cumbre Vieja volcano to 10 km depth and in the southern part of the island at almost any depth. Positive RANs (horizontal bars) are revealed from 10 to 15 km depth below the volcano. The amplitude of Vp RAN in the study area is <5.15% for 95% of the total nodes. Without forgetting the lower resolution obtained for the first cluster, there is a clear shift between the first and second clusters from positive to negative RAN under the volcano from 5 to 13 km (Fig. S10 Images d, e, g and h).

5. Discussion and conclusions

The study area has a long history of volcanism and geothermal activity. This means that anomalies in seismic velocities may be related to changes in lithology, the properties of the rocks, gas content and fluid distribution in the crust. They are also influenced by variations in pressure, temperature, saturation, porosity, etc.

The strong high-Vp anomaly under the Taburiente caldera coinciding with the resistive body (> 103 Ω·m) obtained by Di Paolo et al. (2020, Fig. S11) can be interpreted as the oldest basal complex. Klügel et al. (2005) and Galipp et al. (2006) interpreted this body as a Pliocene seamount and plutonic intrusions. In addition, based on InSAR and GPS observation techniques, Prieto et al. (2009) concluded that the main structural feature of the island was a large central body with high density, which was interpreted as an uplifted seamount from the Pliocene and a relatively dense intrusive plutonic complex/magma body. Simultaneously, Camacho et al. (2009) used 3-D gravity inversion to show that the main anomalous structure detected in La Palma is the central extended density maximum, which corresponds to the intrusive plutonic part of the basal complex outcropping under the Taburiente Caldera. We detected a smaller N-S elongated positive anomaly in the south in accordance with the results obtained by Prieto et al. (2009). D'Auria et al. (2022) conducted a seismic tomography for local earthquakes in the same area that we studied. It is difficult to compare our results with theirs due to the different approaches (in terms of grid space, resolution, methodology and objectives proposed), however it is

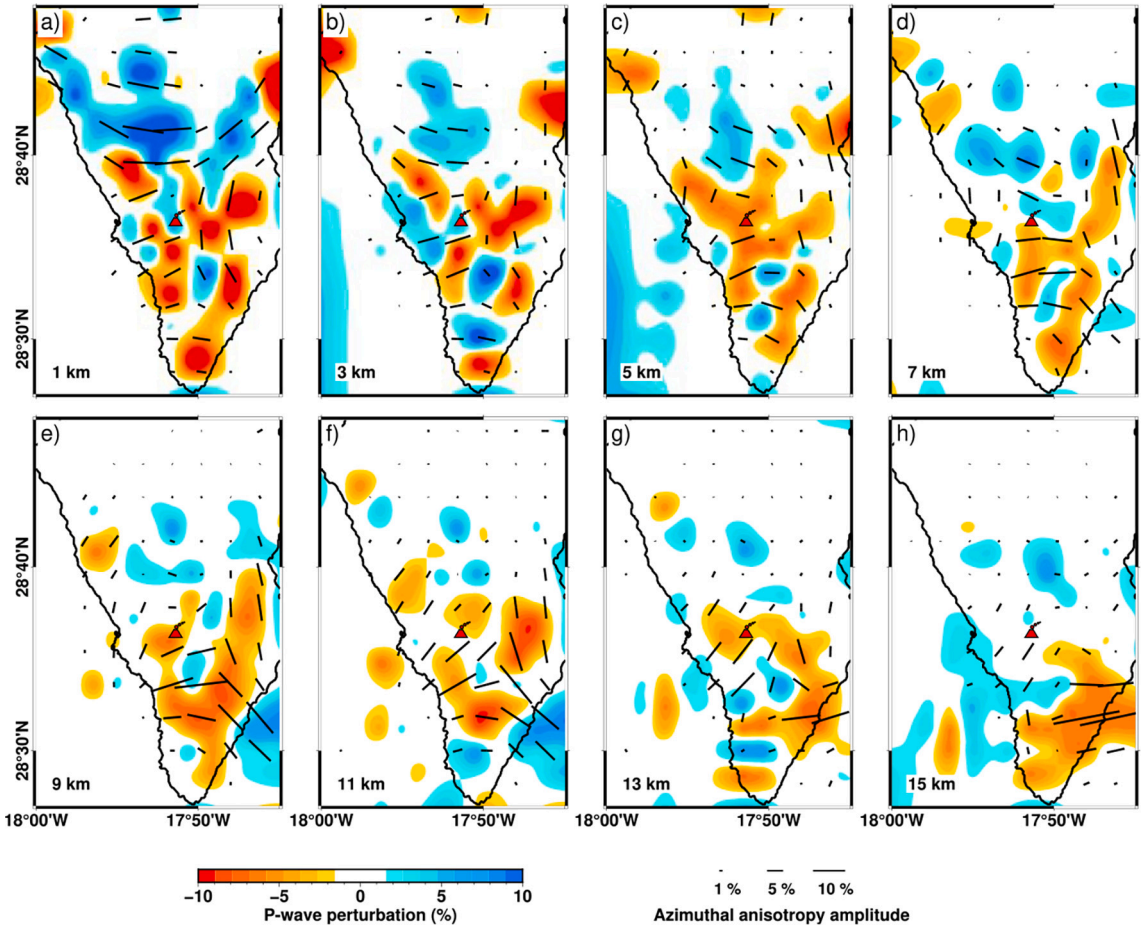

Fig. 9. Map views of Vp azimuthal anisotropy tomography. The layer depth is shown in the bottom-left corner of each map. The red and blue colors indicate low and high isotropic velocities, respectively. The orientation and length of the short black bars indicate the fast-velocity direction (FVD) and the anisotropic amplitude, respectively. The anisotropic amplitude scale is shown at the bottom. (For interpretation of the references to colour in this figure legend, the reader is referred to the web version of this article.)

interesting to note the wide low P-velocity area that they obtained from surface layers to 7–8 km depth in the southern part of Cumbre Vieja, which roughly coincides with our results (for a better comparison it should be noted that our cross sections were orientated S-N while those used by D'Auria et al. (2022) were N-S).

At shallower layers in the southern half of the island, the strong negative anomalies in the N-S direction occupy the same relative position as in the results revealed by Camacho et al. (2009), who associated low-density areas, obtained from a gravity survey, with zones with shallow fractures that could be associated with the N-S rift structure in Cumbre Vieja. From 2 to 4 km depths, Di Paolo et al. (2020) obtained two low-resistivity anomalies in the N-S direction; our results indicate that both anomalies are coincident with two negative seismic anomalies to 3 km depth. Usually a significant fault gouge and/or fracturing with contained fluids show low seismic velocity and low resistivity. In our case, both the electrical and the seismic anomalies around the Cumbre Vieja volcanic ridge could indicate the presence of an active geothermal system. Identified a shallow localized region (< 3 km) of hydrothermal alteration, although the results are difficult to compare due to the different resolutions of the models.

The most interesting result of the inversions for the three datasets is a dramatic change in P-wave seismic velocity, from positive to negative values before and after the eruption in the same area up to 5 km depth (Fig. 5, Images a and b). However, just beneath the active volcano (Images d and e), low velocities are obtained at 1 km depth from the first cluster and high velocities from the second cluster. From 1 to 3 km depths (Fig. 8) we obtained one of the most prominent features of the seismic structure: an elongated Vp/Vs anomaly located beneath the northwestern part of the Cumbre Vieja volcano. We can see high-Vp and low-Vs anomalies that result in very high Vp/Vs ratios of up to 2.2. Unfortunately, we do not have sufficient resolution to compare the evolution of the Vp/Vs ratio before and after the eruption with the changes in Vp due to the increase in shallow seismicity just a few days before the eruption. According to Husen et al. (2000), Vp/Vs is directly related to the Poisson's ratio, which means it is uniquely placed to infer the lithology of rocks. It is also a robust indicator of composition (Christensen, 1996), melt (Walsh, 1968, 1969) and crack distribution (Collier and Singh, 1998), and of the composition and microstructure of magma bodies. Koulakov et al. (2011) suggested that Vp is more sensitive to composition, and that higher Vp values may be an indicator of rocks that came from greater depths. At the same time, very low S-velocity values indicate a high fluids content and partial melting. Kasatkina et al. (2014) presented tomographic models where prominent anomalies with extremely high Vp/Vs ratios (up to 2.4) can be interpreted as magma reservoirs containing high levels of partial melt and/or fluids.

About 88% of the seismic events occur at depths of 6 to 15 km where a finger-shaped anomaly can be observed in the second and third clusters of data dipping to the south with high Vp and Vs values at similar depths (Figs. 5 and S8 Cross-sections B-B′, C-C′ and D-D′). This anomaly is surrounded by low-Vp zones. Fig. 7 shows a low Vp/Vs ratio in the same area. As mentioned earlier, numerous studies indicate that high Vp/Vs ratios in volcanic areas mark the paths taken by fluids and melts that ascend from the deep magma source, although we did not obtain these

results at these depths. According to Kasatkina et al. (2014), during an eruption a large portion of fluids and melts from the deep conduit migrate upward and cause fluid saturation within the summit and a deficit of liquids in deeper parts. This might explain the low Vp/Vs ratios in Cumbre Vieja, however, we should be very careful when making this assertion, in that in the deepest region of our model the resolution is very low before the eruption, although it improves considerably during and after it. We also found, in line with Koulakov et al. (2013), that in the relaxation period following the eruption, the Vp/Vs values were generally low and no strongly anomalous zones could be observed in the crust.

The central-western part of the study area shows that the FVD is mostly *E*-W from 1 to 3 km depth and nearly NE-SW from 9 to 15 km depth. Martinez-Arevalo et al. (2013), using Ps receiver functions, estimated that the Moho varies in depth from 11.5 to 12.5 km beneath La Palma Island. That is, our results just beneath the crust are consistent with the Nubia plate azimuth from the NUVEL-1A model (46.7 ± 0.95° E) that runs parallel to the absolute plate motion (APM) direction of the African plate. Similar results were obtained by Arnoso et al. (2020) and Martín et al. (2014). Also according to Schlaphorst et al. (2023), many sectors in Madeira Island and the western younger Canary Islands (El Hierro, La Palma, La Gomera and Tenerife) show an FPD close to the present-day mantle flow direction. According to Mainprice (2007), from the earliest observations, it was clear that the anisotropy in the upper mantle was caused by the crystal preferred orientation (CPO) of olivine crystal induced by plastic deformation related to mantle flow processes at the geodynamic or plate tectonic scale. The major cause of seismic anisotropy in the upper mantle is the CPO caused by plastic deformation. This means that the anisotropy near the surface can be attributed to the aligned cracks, while that in the lower crust and upper mantle reflects the lattice-preferred orientation (LPO) of minerals (Mainprice, 2007, Karato et al., 2008).

However, we should bear in mind that there is only one permanent GNSS (Global Navigation Satellite System) station on the island, situated in the western part. The FVDs revealed on the eastern flank of the Cumbre Vieja ridge exhibit mainly NW-SE directions from 9 to 11 km depth and turn to E-W in the deepest layers. It is worth noting that from 9 to 15 km depth, there is a significant rotation in the FVD around the Cumbre Vieja axis rift from NE-SW to NW-SE/E-W from west to east in the southern half of the island. The NW-SE/E-W trending fast directions of azimuthal anisotropy are nearly parallel to the extension direction of the rift on the eastern side and similar features have also been observed in other rift regions which show fast azimuths parallel to the extension direction (Vinnik et al., 1992; Gao et al., 1997). As the fast direction should in fact be normal to the extension direction, this topic will have to be studied in greater depth in future research, now that we have a large number of seismic stations on the island and will be able to obtain a better resolution. It is difficult to establish a direct link between the FVDs in the crust and the tectonic stress or surface geology, and the anisotropic patterns we obtained are more likely due to a combination of various different mechanisms. In addition, the anisotropy in the crust due to aligned fractures usually changes a great deal over very short distances (e.g., Huang et al., 2011b).

Using teleseismic and local shear-wave splitting (SWS) measurements, Schlaphorst et al. (2020, 2022) obtained results with important variations in La Palma, although two general patterns could be observed: in the northeast they were close to general plate motion (46.7° E), while in the south of the island they displayed a northwest-southeast direction. All in all, they obtained 26 results for La Palma from 8 stations. In research over the period 2006–2010 using geodetic techniques such as Global Navigation Satellite System (GNSS), Advanced Differential Synthetic Aperture Radar Interferometry (A-DInSAR) and microgravimetry, Escayo et al. (2020) found that, although there were no significant associated variations in gravity, there was a clear surface deformation that varied over time and space.

According to Johnson (2015), crustal SWS in volcanic regions is assumed to be completely due to microcracks aligned with the maximum horizontal compressive stress produced by magma pressure and movement. Under this assumption, the fast anisotropy directions would be radial to overpressurized magma reservoirs and tangential to underpressurized magma reservoirs. At times when the pressure of the magmatic system is lower and the volcano is deflating, the maximum horizontal compressive stress may rotate to be tangential to the center of deformation, and other factors such as aligned fractures in fault zones may assume the dominant role in determining the anisotropy directions. Our results suggest that the anisotropy is mostly governed by pervasive regional and structural characteristics, for example, parallel to the APM direction of the African plate in the western part and almost parallel to the tensional stress direction in the southwestern corner of the island. The FVD distribution might not be correlated with volcanic activity, although the radial anisotropy may be strongly affected.

From our complete data set, negative RAN (i.e. vertical velocity > horizontal velocity) generally appears in the crust under the Cumbre Vieja volcano to 10 km depth and in the southern part of the island at almost any depth. This negative RAN is revealed in the low-V zones although it also appears in high-V areas. This zone is probably caused by local asthenospheric upwelling at shallow depths possibly associated with rift-related lithospheric extension or vertical fracture planes which could also generate negative RAN. Positive RAN (i.e. horizontal velocity > vertical velocity) associated to low-V is revealed from 10 to 15 km depth below the Cumbre Vieja volcano. There is a clear change from positive to negative RAN between the first and second cluster below the volcano from 5 to 13 km, although the low resolution of the model does not allow us to reach definitive conclusions. Our complete inversion results do not seem to show a close connection between the isotropic velocity variation and RAN.

CRediT authorship contribution statement

I. Serrano: Writing – original draft, Investigation. **M.A. Dengra:** Software, Data curation, Visualization. **F.J. Almendros:** Conceptualization, Investigation. **F. Torcal:** Software, Data curation, Investigation. **D. Zhao:** Methodology, Software, Supervision.

Declaration of Competing Interest

The authors declare that they have no known competing financial interests or personal relationships that could have appeared to influence the work reported in this paper.

Data availability

Data will be made available on request.

Acknowledgements

This work has been funded by the following projects: “Visualización de modelos sísmicos temporales generados a partir de la integración de los tiempos de viaje de los terremotos registrados en Andalucía (Junta de Andalucía, P20_00694), BRAVOSEIS CTM2016-77315-R (Spanish Ministry of Science), PID2019-109608GB-I00 (Spanish Ministry of Science) and A-RNM-421-UGR18 (FEDER Junta de Andalucía Consejería de Economía y Conocimiento) and PID2021-124381NB-C21 funded by MCIN/AEI/10.13039/501100011033 and by “ERDF A way of making Europe”. We would like to thank the authors of the paper Di Paolo et al. (2020) for providing us with Fig. S11. Funding for open access charge: Universidad de Granada / CBUA.

Appendix A. Supplementary data

Supplementary data to this article can be found online at https://doi.org/10.1016/j.jvolgeores.2023.107870.

References

Aki, K., Lee, 1976. Determination of three-dimensional velocity anomalies under a seismic array using first P arrival times from local earthquakes: 1. A homogeneous initial model. J. Geophys. Res. 81 (23), 4381–4399. https://doi.org/10.1029/JB081i023p04381.

Albert, H., Costa, F., Martí, J., 2016. Years to weeks of seismic unrest and magmatic intrusions precede monogenetic eruptions. Geology 44 (3), 211–214. https://doi.org/10.1130/G37239.1.

Ancochea, E., Hernán, F., Cendrero, A., Cantagrel, J.M., Fúster, J.M., Ibarrola, E., Coello, J., 1994. Constructive and destructive episodes in the building of a young oceanic Island, La Palma, Canary Islands, and genesis of the Caldera de Taburiente. J. Volcanol. Geotherm. Res. 60, 243–262.

Anderson, D.L., 1989. Theory of the Earth. Blackwell Scientific Publications, Boston. http://resolver.caltech.edu/CaltechBOOK:1989.001.

Arnoso, J., Riccardi, U., Benavent, M., Tammaro, U., Montesinos, F.G., Blanco-Montenegro, I., Vélez, E., 2020. Strain pattern and kinematics of the Canary Islands from GNSS time series analysis. Remote Sens. 12 (20), 3297. https://doi.org/10.3390/rs12203297.

Backus, G.E., 1965. Possible forms of seismic anisotropy of the uppermost mantle under oceans. J. Geophys. Res. 70 (14), 3429–3439. https://doi.org/10.1029/JZ070i014p03429.

Barker, A.K., Troll, V.R., Carracedo, J.C., Nicholls, P.A., 2015. The magma plumbing system for the 1971 Teneguía eruption on La Palma, Canary Islands. Contrib. Mineral. Petrol. 170, 54 (2015). https://doi.org/10.1007/s00410-015-1207-7 (2015).

Cabrera-Perez, I., D'Auria, L., Soubestre, J., Barrancos, J., Padilla, G.D., Perez, N.M., 2021. A nonlinear multiscale inversion approach for ambient noise tomography. Geophys. J. Int. 225, 1158–1173. https://doi.org/10.1093/gji/ggaa574.

Camacho, A.G., Ferna'ndez, J., Gonza'lez, P.J., Rundle, J.B., Prieto, J.F., Arjona, A., 2009. Structural results for La Palma island using 3-D gravity inversion. J. Geophys. Res. 114, B05411. https://doi.org/10.1029/2008JB005628.

Carracedo, J.C., Badiola, E.R., Guillou, H., De la Nuez, J., Pérez-Torrado, F.J., 2001. Geology and volcanology of La Palma and El Hierro, Western Canaries. Estud. Geol. 57, 175–273.

Carracedo, J.C., Troll, V.R., Day, J.M.D., Geiger, H., Aulinas, M., Soler, V., et al., 2022. The 2021 eruption of the Cumbre Vieja volcanic ridge on La Palma, Canary Islands. Geol. Today 38, 94–107. https://doi.org/10.1111/gto.12388.

Chouet, B.A., Matoza, R.S., 2013. A multi-decadal view of seismic methods for detecting precursors of magma movement and eruption. J. Volcanol. Geotherm. Res. 252, 108–175. https://doi.org/10.1016/j.jvolgeores.2012.11.013.

Christensen, N.I., 1996. Poisson's ratio and crustal seismology. J. Geophys. Res. Solid Earth 101 (B2), 3139–3156.

Civico, R., Ricci, T., Scarlato, P., Taddeucci, J., Andronico, D., Del Bello, E., D'Auria, L., Hernández, P.A., Pérez, N.M., 2022. High-resolution digital surface model of the 2021 eruption deposit of Cumbre Vieja volcano, La Palma, Spain. Sci. Data 9, 435. https://doi.org/10.1038/s41597-022-01551-8.

Collier, J.S., Singh, S.C., 1998. Poisson's ratio structure of young oceanic crust. J. Geophys. Res. Solid Earth 103 (B9), 20981–20996.

Dañobeitia, J.J., 1980. Interpretación de la estructura de la corteza en el Archipiélago Canario a partir de perfiles sísmicos profundos de refracción. Ph.D. Thesis. Universidad Complutense de Madrid, p. 91.

D'Auria, L., Koulakov, I., Prudencio, J., Cabrera-Pérez, I., Ibáñez, J.M., Barrancos, J., et al., 2022. Rapid magma ascent beneath La Palma revealed by seismic tomography. Sci. Rep. 12, 17654. https://doi.org/10.1038/s41598-022-21818-9.

De Plaen, R.S.M., Mordret, A., Arambula-Mendoza, R., Vargas-Bracamontes, D., Marquez-Ramirez, V.H., Lecocq, T., et al., 2022. The shallow three-dimensional structure of Volcan de Colima revealed by ambient seismic noise tomography. J. Volcanol. Geotherm. Res. 428, 107578. https://doi.org/10.1016/j.jvolgeores.2022.107578.

Di Paolo, et al., 2020. La Palma island (Spain) geothermal system revealed by 3D magnetotelluric data inversion. Sci. Rep. 10, 18181. https://doi.org/10.1038/s41598-020-75001-z.

Eberhart-Phillips, D., 1986. Three-dimensional velocity structure in Northern California Coast Ranges from inversion of local earthquake arrival times. Bull. Seismol. Soc. Am. 76, 1025–1052.

Eberhart-Phillips, D., Henderson, C., 2004. Including anisotropy in 3-D velocity inversion and application to Marlborough, New Zealand. Geophys. J. Int. 156, 237–254.

Escayo, J., Fernandez, J., Prieto, J.F., Camacho, A.G., Palano, M., Aparicio, A., Rodriguez-Velasco, G., Ancochea, E., 2020. Geodetic study of the 2006-2010 ground deformation in La Palma (Canary Islands): observational results. Remote Sens. 12 (16), 2566. https://doi.org/10.3390/rs12162566.

Fernandez, J., Escayo, J., Hu, Z., Camacho, A.G., Samsonov, S.V., Prieto, J.F., et al., 2021. Detection of volcanic unrest onset in La Palma, Canary Islands, evolution and implications. Sci. Rep. 11, 2540. https://doi.org/10.1038/s41598-021-82292-3.

Fichtner, A., 2010. Full Seismic Waveform Modelling and Inversion. Springer Science & Business Media.

Galipp, K., Klügel, A., Hansteen, T.H., 2006. Changing depths of magma fractionation and stagnation during the evolution of an oceanic island volcano: La Palma (Canary Islands). J. Volcanol. Geotherm. Res. 155 (3–4), 285–306.

Gao, S., Davis, P.M., Liu, H., Slack, P.D., Rigor, A.W., Zorin, Y.A., Logatchev, N.A., 1997. SKS splitting beneath continental rift zones. J. Geophys. Res. Solid Earth 102 (B10), 22781–22797.

Geiger, L., 1910. Herbsetimmung bei Erdbeben aus den Ankunfzeiten. K. Gessell. Wiss. Goett. 4, 331–349.

Geiger, L., 1912. Probability method for the determination of earthquake epicenters from the arrival time only. Bull. St. Louis Univ. 8, 60–71.

Gerst, A., Savage, M.K., 2004. Seismic anisotropy beneath Ruapehu Volcano: a possible eruption forecasting tool. Science 306, 1543–1547. https://doi.org/10.1126/science.1103445.

Hsin-Hua, Huang, et al., 2015. The Yellowstone magmatic system from the mantle plume to the upper crust. Science 348, 773–776. https://doi.org/10.1126/science.aaa5648.

Hudson, T.S., Kendall, J.M., Blundy, J.D., Pritchard, M.E., MacQueen, P., Wei, S.S., et al., 2023. Hydrothermal fluids and where to find them: using seismic attenuation and anisotropy to map fluids beneath Uturuncu Volcano, Bolivia. Geophys. Res. Lett. 50 https://doi.org/10.1029/2022GL100974 e2022GL100974.

Husen, S., Kissling, E., Flueh, E.R., 2000. Local earthquake tomography of shallow subduction in North Chile: a combined onshore and offshore study. J. Geophys. Res. Solid Earth 105 (B12), 28183–28198.

Ishise, M., Kawakatsu, H., Shiomi, K., 2012. Revision of the 3-D anisotropic velocity structure of the Japan islands using Hi-net data: Northeastern Japan, B12–2. In: Programme and Abstracts of the 2012 Fall Meeting of Seismological Society of Japan, Hakodate, Japan.

Jiang, C., Schmandt, B., Farrell, J., Lin, F.-C., Ward, K.M., 2018. Seismically anisotropic magma reservoirs underlying silicic calderas. Geology 46, 727–730. https://doi.org/10.1130/G45104.1.

Johnson, J.H., 2015. Seismic anisotropy in volcanic regions. In: Beer, M., Kougioumtzoglou, I.A., Patelli, E., Au, S.-K. (Eds.), Encyclopedia of Earthquake Engineering. Springer, pp. 2692–2706. https://doi.org/10.1007/978-3-642-35344-4_44.

Kasatkina, E., Koulakov, I., West, M., Izbekov, P., 2014. Seismic structure changes beneath Redoubt Volcano during the 2009 eruption inferred from local earthquake tomography. J. Geophys. Res. Solid Earth 119 (6), 4938–4954.

Kawakatsu, H., 2016. A new fifth parameter for transverse isotropy. Geophys. J. Int. 204 (1), 682–685.

Klügel, A., Hansteen, T.H., Galipp, K., 2005. Magma storage and underplating beneath Cumbre Vieja volcano, la Palma (Canary Islands). Earth Planet. Sci. Lett. 236 (1–2), 211–226.

Koulakov, I., Shapiro, N., 2015. Seismic tomography of volcanoes. In: Beer, M., Kougioumtzoglou, I.A., Patelli, E., Au, S.-K. (Eds.), Encyclopedia of Earthquake Engineering. Springer, pp. 3117–3134. https://doi.org/10.1007/978-3-642-35344-4_51.

Koulakov, I., Jakovlev, A., Luehr, B.G., 2009. Anisotropic structure beneath Central Java from local earthquake tomography. Geochem. Geophys. Geosyst. 10 https://doi.org/10.1029/2008GC002109.

Koulakov, I., Gordeev, E.I., Dobretsov, N.L., Vernikovsky, V.A., Senyukov, S., Jakovlev, A., 2011. Feeding volcanoes of the Kluchevskoy group from the results of local earthquake tomography. Geophys. Res. Lett. 38 (9).

Koulakov, I., Gordeev, E.I., Dobretsov, N.L., Vernikovsky, V.A., Senyukov, S., et al., 2013. Rapid changes in magma storage beneath the Klyuchevskoy group of volcanoes inferred from time-dependent seismic tomography. J. Volcanol. Geotherm. Res. 263, 75–91. https://doi.org/10.1016/j.jvolgeores.2012.10.014.

Lees, J.M., 2007. Seismic tomography of magmatic systems. J. Volcanol. Geotherm. Res. 167, 37–56. https://doi.org/10.1016/j.jvolgeores.2007.06.008.

Lin, G., Shearer, P.M., Hauksson, E., Thurber, C.H., 2007. A three-dimensional crustal seismic velocity model forsouthern California from a composite event method. J. Geophys. Res. 112, B11306. https://doi.org/10.1029/2007JB004977.

Llsley-Kemp, F., Greenfield, T., Keir, D., 2018. Seismic anisotropy reveals a dynamic link between adjacent magmatic segments prior to Dyke intrusion. J. Geophys. Res. Solid Earth 123, 9800–9816. https://doi.org/10.1029/2018JB016420.

Lo Bue, R., Faccenda, M., Cocina, O., Rappisi, F., Vanderbeek, B.P., 2023. Joint Active and Passive P-Wave Tomography Reveals Mt. Etna's Seismic Anisotropy. EGU General Assembly, EGU23–8563. https://doi.org/10.5194/egusphere-egu23-8563.

Lu, H., Lei, J., Zhao, D., Xu, Y.-G., Sun, C., Hu, X., 2022. Pn anisotropic tomography of Hainan Island and surrounding areas: new insights into the Hainan Mantle Plume. J. Geophys. Res. Solid Earth 127. https://doi.org/10.1029/2021JB023609 e2021JB023609.

Mainprice, David, 2007. Seismic Anisotropy of the Deep Earth from a Mineral and Rock Physics Perspective. https://doi.org/10.1016/B978-044452748-6/00045-6.

Martín, A., Sevilla, M., Zurutuza, J., 2014. Crustal deformation study in the Canary Archipelago by the analysis of GPS observations. J. Appl. Geod. 8 (2), 129–140.

Mordret, A., Rivet, D., Landes, M., Shapiro, N.M., 2015. Three-dimensional shear velocity anisotropic model of Piton de la Fournaise Volcano (La Réunion Island) from ambient seismic noise. J. Geophys. Res. Solid Earth 120, 406–427. https://doi.org/10.1002/2014JB011654.

Nettles, M., Dziewoński, A.M., 2008. Radially anisotropic shear velocity structure of the upper mantle globally and beneath North America. J. Geophys. Res. Solid Earth 113 (B2).

Padrón, E., Pérez, N.M., Rodríguez, F., Melián, G., Hernández, P.A., Sumino, H., et al., 2015. Dynamics of diffuse carbon dioxide emissions from Cumbre Vieja volcano, La Palma, Canary Islands. Bull. Volcanol. 77, 28. https://doi.org/10.1007/s00445-015-0914-2.

Perton, M., Maldonado-Hernandez, L.T., Figueroa-Soto, A., Sosa-Ceballos, G., De Jesus-Amador, J., Angulo, J., Calo, M., 2022. The magmatic plumbing system of the Acoculco volcanic complex (Mexico) revealed by ambient noise tomography. J. Volcanol. Geotherm. Res. 432, 107704. https://doi.org/10.1016/j.jvolgeores.2022.107704.

Prieto, J.F., González, P.J., Seco, A., Rodríguez-Velasco, G., Tunini, L., Perlock, P.A., Fernández, J., et al., 2009. Geodetic and structural research in La Palma, Canary Islands, Spain: 1992–2007 results. Pure Appl. Geophys. 166 (8), 1461–1484.

Raitt, R.W., Shor Jr., G.G., Francis, T.J.G., Morris, G.B., 1969. Anisotropy of the Pacific upper mantle. J. Geophys. Res. 74 (12), 3095–3109.
Romero Ruiz, C., 1989. Las manifestaciones volcánicas históricas del archipiélago canario. PhD Thesis. University of La Laguna.
Romero, J.E., Burton, M., Caceres, F., Taddeucci, J., Civico, R., Ricci, T., et al., 2022. The initial phase of the 2021 Cumbre Vieja ridge eruption (Canary Islands): products and dynamics controlling edifice growth and collapse. J. Volcanol. Geotherm. Res. 431, 107642. https://doi.org/10.1016/j.jvolgeores.2022.107642.
Saade, M., Araragi, K., Montagner, J.P., Kaminski, E., Roux, P., Aoki, Y., Brenguier, F., 2019. Evidence of reactivation of a hydrothermal system from seismic anisotropy changes. Nat. Commun. 10, 5278. https://doi.org/10.1038/s41467-019-13156-8.
Schlaphorst, D., Silveira, G., Mata, J., 2020. Investigating Seismic Anisotropy of the Madeira and Canaries Hotspots Using Teleseismic and Local Shear-Wave Splitting with the SIGHT project. D1503 | EGU2020-9340.
Schlaphorst, D., Silveira, G., Mata, J., Krüger, F., Dahm, T., Ferreira, A.M.G., April 2023. Heterogeneous seismic anisotropy beneath Madeira and Canary archipelagos revealed by local and teleseismic shear wave splitting. Geophys. J. Int. 233 (1), 510–528. https://doi.org/10.1093/gji/ggac472.
Spica, Z., Perton, M., Legrand, D., 2017. Anatomy of the Colima volcano magmatic system, Mexico. Earth Planet. Sci. Lett. 459 (2), 1–13.
Staudigel, H., Schmincke, H.-U., 1984. The Pliocene seamount series of La Palma, Canary Islands. J. Geophys. Res. 89, 11195–11215.
Thomsen, L., 1986. Weak elastic anisotropy. Geophysics 51 (10), 1954–1966.
Torres-Gonzalez, P.A., Luengo-Oroz, N., Lamolda, H., D'Alessandro, W., Albert, H., Iribarren, I., Moure-Garcia, D., Soler, V., 2020. Unrest signals after 46 years of quiescence at Cumbre Vieja, La Palma, Canary Islands. J. Volcanol. Geotherm. Res. 392, 106757. https://doi.org/10.1016/j.jvolgeores.2019.106757.
Troll, V.R., Carracedo, J.C., 2016. The geology of La Palma. In: The Geology of the Canary Islands. Elsevier, pp. 101–180. https://doi.org/10.1016/B978-0-12-809663-5.00003-7.Walsh, 1968, 1969.
Walsh, B., 1968. Attenuation in partially melted materialJ. Geophys. Res. 73, 2209–2216.
Walsh, J.B., 1969. New analysis of attenuation in partially melted rockJ. Geophys. Res. 74, 4333–4337.
Wang, J., Zhao, D., 2008. P-wave anisotropic tomography beneath Northeast Japan. Phys. Earth Planet. Inter. 170, 115–133.
Wang, J., Zhao, D., 2013. P-wave tomography for 3-D radial and azimuthal anisotropy of Tohoku and Kyushu subduction zones. Geophys. J. Int. 193, 1166–1181. https://doi.org/10.1093/gji/ggt086.
Yuan, H.Y., Romanowicz, B., Fischer, K.M., Abt, D., 2011. 3-D shear wave radially and azimuthally anisotropic velocity model of the North American upper mantle. Geophys. J. Int. 184 (3), 1237–1260.
Zhao, D., 2015. Multiscale Seismic Tomography. Springer, p. 304.
Zhao, D., Hasewaga, A., Horiuchi, S., 1992. Tomographic imaging of P and S wave velocity structure beneath northeastern Japan. J. Geophys. Res. 97, 19909–19928.
Zhao, D., Hua, Y., 2021. Anisotropic tomography of the Cascadia subduction zone. Phys. Earth Planet. Inter. 318, 106767.
Konstantinou, K.I., Perwita, C.A., Maryanto, S., Surono, Budianto, A., Hendrasto, M., 2013. Maximal Lyapunov exponent variations of volcanic tremor recorded during explosive and effusive activity at Mt Semeru volcano, Indonesia, Nonlin. Processes Geophys. 20, 1137–1145. https://doi.org/10.5194/npg-20-1137-2013.
Hearn, T.M., 1996. Anisotropic Pn tomography in the western United States. J. Geophys. Res. 101 (B4), 8403–8414.
Martinez-Arevalo, C., Mancilla, F., Helffrich, G., Garcia, A., 2013. Seismic evidence of a regional sublithospheric low velocity layer beneath the Canary Islands. Tectonophysics 608, 586–599. https://doi.org/10.1016/j.tecto.2013.08.021.
Karato, S., Jung, H., Katayama, I., Skemer, P., 2008. Significance of Seismic Anisotropy of the Upper Mantle: New Insights from Laboratory Studies. Annu. Rev. Earth Planet Sci. 36 (1), 59–95.
Vinnik, L.P., Makeyeva, L.I., Milev, A., Usenko, A.Y., 1992. Global patterns of azimuthal anisotropy and deformations in the continental mantle. Geophys. J. Int. 111, 433–447.